Advanced Fault Diagnosis Method for DC-DC Converters: Leveraging the Temporal Continuity of Electrical Signals

Li Wang, Zidong Wang, *Fellow, IEEE*, Chao Xu, Yiming Xu and Liang Hua

***Abstract*—This paper focuses on the crucial role of reliable DC-DC converter operation for the stability of modern power electronic devices. Addressed is a common issue in the fault diagnosis of DC-DC converters: the tendency to rely on local feature fitting while the temporal continuity of electrical signals is neglected. An innovative diagnostic method that utilizes an Adaptive Wavelet Transform (AWT) from a data processing perspective is proposed. This technique can dynamically adjust the scale and translation parameters to adapt to the continuous changes in electrical signals caused by varying circuit conditions. From the standpoint of model improvement, the Extended Convolutional Capsule Network (XCCN) model is designed. Through multi-scale feature extraction, integration of global-local attention mechanisms, and global vector analysis, this model effectively diagnoses fault features. It is demonstrated that our method is effective in extracting the time-continuity features of electrical signals, and exhibits significant advantages in diagnostic accuracy, performance metrics, and application generalisation capability. Consequently, this study presents a holistic and effective approach for fault diagnosis in DC-DC converters.**

***Index Terms*—Fault diagnosis, DC-DC converter, hidden fault, adaptive wavelet transform, capsule network.**

I. Introduction

SWITCHING power converters, notably those of the DC-DC type, are pivotal for electronic systems and are extensively utilized in areas such as renewable energy systems, electric vehicles, and computer power management [1]. The performance of these systems is directly influenced by the reliability of these converters. As a result, fault diagnosis, particularly of hidden faults caused by changes in component parameters, has emerged as a significant area of research [2]. The rapid development of machine learning technology has led to an increasing number of studies employing this sophisticated technique for the diagnosis of hidden faults in DC-DC converters [3]. Current research primarily concentrates on two aspects: data processing methods and techniques for model improvement.

Data processing methods are aimed at enhancing the accuracy of fault diagnosis by improving both the quantity and quality of the collected data [4]. For example, literature [5] presents a method using Generative Adversarial Networks (GAN) to simulate circuit fault diagnosis. This approach enriches training data by combining original data with data generated by the GAN. Another study [6] introduces a method employing Cross Wavelet Transform (XWT) to convert one-dimensional signals into two-dimensional images, effectively increasing the data dimensions. Moreover, a Sensitive Feature Mahalanobis Distance (SFMD) extraction method has been proposed in [7], tailored for pre-identifying key fault features in analog circuits. However, a common limitation of these methods is their lack of consideration for the temporal continuity of electrical signals during the data processing stage, leading to data being processed in a discrete manner [8]. This oversight can result in the loss of continuity features at the initial feature extraction phase, potentially impacting the overall efficacy of fault diagnosis.

Model improvement methods focus on boosting fault diagnosis performance by refining model architecture and modifying iteration strategies [9]. For instance, a technique utilizing one-dimensional Convolutional Neural Networks (CNN) has been investigated in [10] to analyze temporal data, enabling fault detection by evaluating the output data from test circuits. In [11], an innovative approach has been introduced that combines the Short-Time Fourier Transform with ResNet networks. Moreover, an advanced fault diagnosis method has been presented in [12] by employing a multi-level fusion network based on the inception architecture. This method creates a comprehensive feature extraction framework by integrating convolutional kernels of different sizes at the input layer. Lastly, a fault diagnosis strategy has been detailed in [13] [14] by incorporating transfer learning, which significantly enhances the ability to recognize offset fault features, especially in response to variations in the distribution of fault data.

The aforementioned models primarily rely on CNNs to enhance fault diagnosis capabilities. In processing electrical signals, they achieve classification and diagnosis through the convolutional segmentation and pooling of data [15]. This method, based on convolutional kernels, focuses mainly on local feature matching and overlooks the temporal continuity of analog circuit signals [16] [17]. This limitation results in the model performing poorly in practical circuit applications due to its sensitivity to local variations. Specifically, it is prone to misjudgments when the operational state or load of the circuit changes.

To address the issues discussed above, this paper introduces a novel approach that specifically focuses on the temporal continuity of electrical signals in DC-DC converters. We pro-

This work was supported in part by the National Natural Science Foundation of China under Grant 62103205 and the Jiangsu Province Scientific and Technological Achievements Transformation Project of China under Grant BA2022026. *(Corresponding author: Liang Hua)*

Li Wang, Chao Xu, Yiming Xu and Liang Hua are with the School of Electrical Engineering and Automation, Nantong University, Nantong 226019, China (e-mails: lwee@ntu.edu.cn; xcxiaoyao@stmail.ntu.edu.cn; yimingx@ntu.edu.cn; hualiang@ntu.edu.cn).

Zidong Wang is with the Department of Computer Science, Brunel University London, UB8 3PH Uxbridge, U.K. (e-mail: Zidong.Wang@brunel.ac.uk).

pose an innovative Extended Convolutional Capsule Network (XCCN) strategy for fault detection. On the data processing level, an Adaptive Wavelet Transform (AWT) technique has been developed, tailored to effectively capture the continuous features of electrical signals. For model improvement, we employ a design based on Capsule Networks (CCN), which excels in conducting global feature analysis, thereby significantly enhancing the accuracy of fault detection [18].

The primary contributions of this study are outlined as follows:

1) *AWT Method Design*: This paper presents an innovative approach to overcoming the scale parameter limitations inherent in the Continuous Wavelet Transform (CWT). By introducing a dynamic parameter adjustment mechanism that leverages Empirical Mode Decomposition (EMD) and Hilbert-Huang Transform (HHT), the method achieves adaptability in scale and shift parameters for different state signals.
2) *XCCN Model Improvement*: A key development in this paper is the MishXception module, which substantially enhances the model's ability to extract features. Additionally, the integration of the CloFormer mechanism markedly improves the model's capacity to process both global and local features comprehensively.
3) *Dual Loss Function*: In this study, a reconstruction loss function is constructed based on the Maximum Mean Discrepancy (MMD) theory. By introducing three types of kernel functions, we enhance the importance of global features during the model's iterative learning process. The reconstruction loss complements the Margin Loss, further boosting the overall performance of the model.

II. Data processing analysis

A. DC-DC Converter Hidden Fault Characteristics

To thoroughly investigate the hidden fault characteristics of DC-DC converters, this study extends the analysis starting from second-order Buck converters, with their circuit topology shown in Fig. 1.

The operating principle of the Buck converter is as follows. When the switch device is on, the inductor starts charging, leading to an increase in the inductor current. When the switch device is off, the inductor discharges its energy to the output capacitor and load, resulting in a decrease in inductor current. Assuming the current i_L flowing out of the inductor remains dynamically stable when outputting to the load, this dynamic inductor current i_L passing through output capacitor C_o will produce a voltage ripple V_{ro}. This voltage ripple consists of two parts: one is the voltage change across the ideal capacitor C, and the other is the voltage drop across the Equivalent Series Resistance (ESR) of C. The formula is as follows:

$$V_{ro} = \Delta V_C + \Delta V_{ESR} = \Delta i_{in}\left(ESR + \frac{1}{8 \cdot f_s \cdot C}\right) \quad (1)$$

It is evident that the total output voltage ripple V_{ro} is influenced by i_L, C, ESR, and switching frequency f_s. Among these factors, the ESR of the output capacitor and the inductor current i_L have the most significant impact.

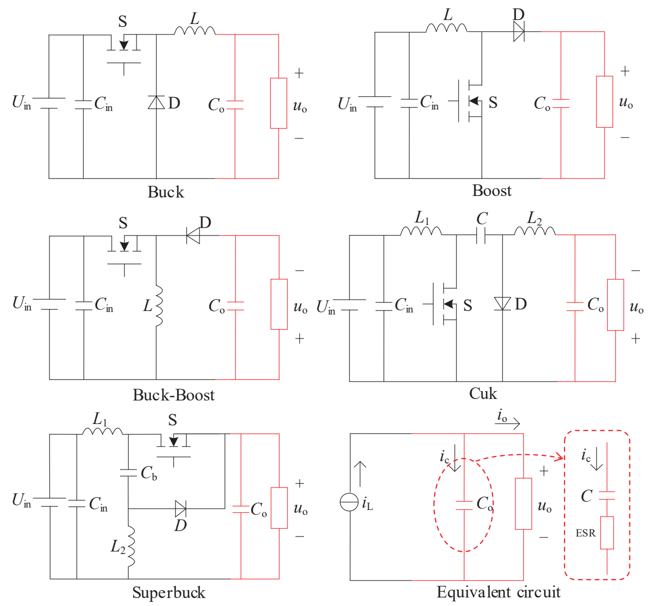

Fig. 1: DC-DC converters equivalent analysis.

Further, this conclusion can be extended to other DC-DC converter topologies, including Boost converters, Buck-Boost converters, Cuk converters, and fourth-order Superbuck converters. As illustrated by the equivalent circuit in Fig. 1, the outputs of these converters can all be represented as current source circuits. The primary differences lie in the sources of current flowing to the output capacitor during each switching cycle.

In summary, by analyzing the output voltage ripple of a power supply, we can detect the aging condition of its components. The output voltage ripple exhibits dual temporal continuity. The changes in the high-frequency part are synchronized with the switching frequency, while the low-frequency part relates to the overall steady-state characteristics of the converter system. This characteristic dictates that a complete temporal continuity must be incorporated when analyzing the output signals of DC-DC converters to accurately represent their data features.

B. Adaptive Wavelet Transform

When analyzing hidden faults in DC-DC converters, the temporal signals often exhibit distinct non-linear and time-varying characteristics. These characteristics make it challenging for traditional signal processing methods to accurately capture the key fault features in the signals. The Continuous Wavelet Transform (CWT) is considered as an effective analytical tool due to its unique advantages in time-frequency analysis [19]. The standard definition of CWT is:

$$CWT_x = \frac{1}{\sqrt{|a|}} \int x(t)\psi\left(\frac{t-b}{a}\right) dt \quad (2)$$

where $x(t)$ is the input signal, ψ is the wavelet basis function, a is the scale parameter, and b is the translation parameter.

The direct application of the CWT in the data processing phase of this study does not fully address the challenges outlined in the introduction. The traditional CWT relies on predetermined parameters 'a' (scale) and 'b' (translation), leading to a uniformity in scale that cannot adapt to the continuous variations in the signal caused by changes in circuit conditions.

To address this issue, our study proposes an adaptive wavelet transform, incorporating a dynamic parameter adjustment mechanism based on EMD [20] and HHT. Through this mechanism, our method is capable of dynamically adjusting the scale and translation parameters to more accurately align with the characteristics of the input signal. This adaptability is key to effectively capturing and representing the subtle variations and crucial features in the output signals of DC-DC converters. The methodology is described as follows.

Firstly, we use EMD to decompose the input signal into a set of Intrinsic Mode Functions (IMFs). Each IMF captures the characteristics of the signal at a specific scale. The formula is given by

$$x(t) = \sum_{n=1}^{N} IMF_n(t) + R(t) \tag{3}$$

where $IMF_n(t)$ represents the nth Intrinsic Mode Function, $R(t)$ is the residual trend term, and N is the number of IMFs. Subsequently, for each $IMF_n(t)$, an HHT of the analytic signal is constructed. The formula is as follows:

$$H(IMF_n(t)) = \frac{1}{\pi} P \cdot V \cdot \int_{-\infty}^{\infty} \frac{IMF_n(\tau)}{t-\tau} d\tau. \tag{4}$$

Here, $P.V.$ denotes the principal value (Cauchy principal value) integral and τ denotes the integral variable. At this point, the amplitude $a_n(t)$ and phase $\theta_n(t)$ of the target signal can be obtained as follows:

$$a_n(t) = \sqrt{IMF_n(t)^2 + H(IMF_n(t))^2} \tag{5}$$

$$\theta_n(t) = \arctan\left(\frac{H(IMF_n(t))}{IMF_n(t)}\right) \tag{6}$$

The local energy $E_l(t)$ and instantaneous frequency $F_c(t)$ can be calculated using the amplitude and frequency. The formulas are as follows:

$$E_l(t) = a_n(t)^2 \tag{7}$$

$$F_c(t) = \frac{1}{2\pi} \frac{d\theta_n(t)}{dt} \tag{8}$$

Subsequently, the scale parameter a and the translation parameter b are dynamically adjusted based on the local energy $E_l(t)$ and the instantaneous frequency $F_c(t)$ as follows:

$$a(t) = \alpha / F_c(t) \tag{9}$$

$$b(t) = t - \beta \cdot \mathrm{sgn}(\frac{dE_l(t)}{dt}) \cdot \sqrt{|E_l(t)|} \tag{10}$$

Here, α and β are adjustable parameters used to control the sensitivity of scale and translation (experimental values: $\alpha = 1, \beta = 0.3$), respectively, sgn represents the direction function given as follows:

$$\mathrm{sgn}(x) = \begin{cases} 1 & x < 0 \\ 0 & x = 0 \\ -1 & x > 0 \end{cases} \tag{11}$$

Finally, the dynamically adjusted parameters $a(t)$ and $b(t)$ are incorporated into the CWT, resulting in the following improvements:

$$AWT_x = \frac{1}{\sqrt{|a(t)|}} \int x(\tau) \psi(\frac{\tau - b(t)}{a(t)}) d\tau \tag{12}$$

The AWT method precisely captures the time-frequency dynamics of the input signal. For the scale parameter $a(t)$, it automatically increases when the input signal's frequency is low, to better capture low-frequency global characteristics; conversely, when the signal's frequency is high, the scale parameter automatically decreases, refining the capture of high-frequency local features. Regarding the translation parameter $b(t)$, AWT reduces the adjustment magnitude when the signal is stable, ensuring that the overall translation of the signal remains smooth. Conversely, when there are abrupt changes in the signal, AWT adjusts $b(t)$ towards the direction of significant energy changes to enhance the temporal resolution near the points of change.

III. Model Improvement Analysis

After data processing with AWT, the output signal is encapsulated in continuous time-frequency images, necessitating the design of a network model capable of analyzing global features. This study has improved upon the capsule network, enhancing the model's ability to extract and utilize global features. Fig. 2 illustrates the structure of the improved model. This model, based on the original capsule network, incorporates advancements like multi-scale convolution MishXception module, Cloformer module, and global reconstruction module.

A. MishXception Module

In this study, recognizing that capsule vector neurons are not inherently capable of directly extracting features from input data, we have designed a specialized module to address this limitation. As depicted in Fig. 2, the MishXception module, inspired by the Xception architecture, is introduced to act as a pre-extraction module for the capsule network. The design of this module includes specific improvements aimed at enhancing its feature extraction capabilities, ensuring that it effectively prepares the data for subsequent processing by the capsule network. The details of these improvements are as follows.

- *Dual-Layer Convolution*: At the input end, three different sizes of dual-layer depthwise separable convolutions(DSconv) are performed in parallel, along with a max pooling operation. This enhances the model's feature extraction performance at small local, medium local, and global levels.
- *Mish Activation Function*: In the early stages of feature extraction, to retain more effective information, we replace ReLU with Mish as the activation function for depthwise separable convolutions. The Mish function exhibits a linear-like increase when $x > 0$, but is not completely zero when $x \leq 0$, rather it approaches zero. This allows for a smoother gradient flow, enabling deeper penetration of information into the neural network.
- *Residual Connections*: As multi-layer, multi-scale convolutions progress, the initial features of the input are prone to information deviation during propagation. To address

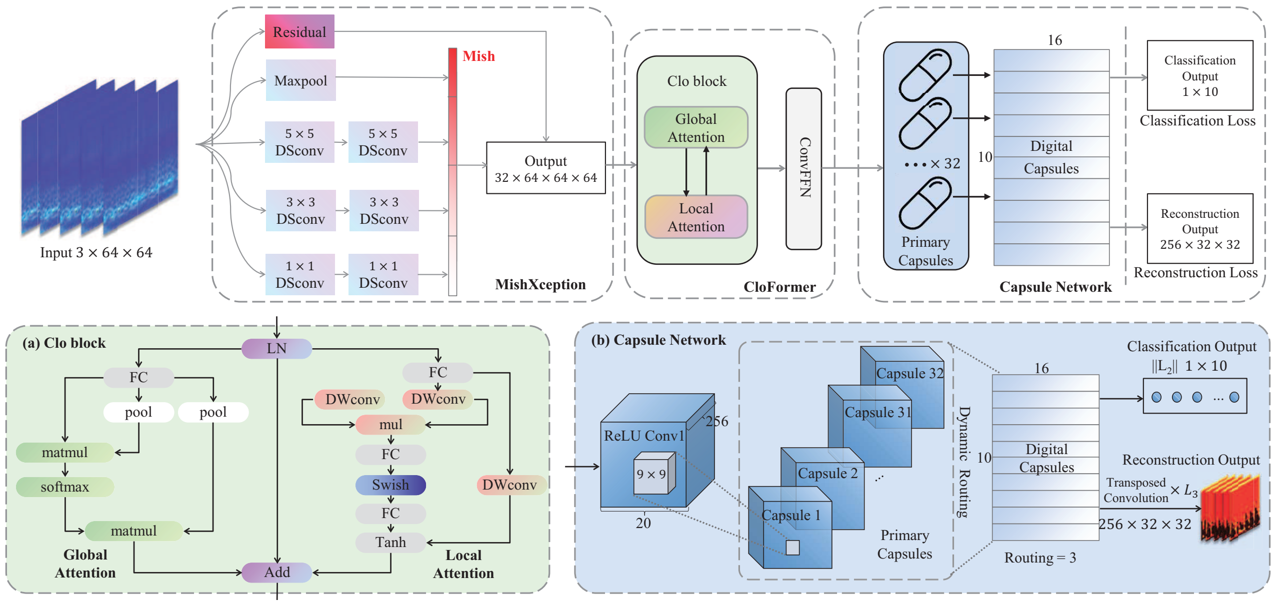

Fig. 2: The developed XCCN with new structure framework.

this, we have introduced residual connections, which add the input directly to the output, ensuring the expressive capability of the output features.

B. Cloformer Module

The CloFormer module, as illustrated in Fig. 2, is a new hybrid attention mechanism comprised of Clo blocks and ConvFFN [21]. This method efficiently achieves the fusion and attention of both global and local features.

The Clo block serves as a hybrid attention module. The global attention computes attention over the entire input, while the local attention performs attention calculations within a fixed-size window on localized areas.

Global attention is achieved by downsampling Key (K) and Value (V) using an average pooling layer. Then, attention scores are calculated using Query (Q) and the downsampled K. Subsequently, these scores are used to weight the downsampled V, resulting in a low-frequency global attention output. The specific formulas are as follows:

$$X_{\text{global}} = \text{Attntion}\left(Q_g, \text{Pool}\left(K_g\right), \text{Pool}\left(V_g\right)\right) \tag{13}$$

Local attention aggregates local information by applying depthwise convolution (DWConv) to the Q and K within the window. Furthermore, the introduction of $Tanh$ and Swish non-linear operators enables stronger context-aware weighting. The specific formulas are as follows:

$$\begin{aligned} Q_l &= \mathbf{DW}\,\text{conv}(Q) \\ K_l &= \mathbf{DW}\,\text{conv}(K) \\ A_{ttn_t} &= \mathbf{FC}\left(\text{Swish}\left(\mathbf{FC}\left(Q_l \odot K_l\right)\right)\right) \\ Attn &= \text{Tanh}\left(\frac{\text{Attn}_t}{\sqrt{d}}\right) \\ X_{\text{local}} &= \text{Attn} \odot V_s \end{aligned} \tag{14}$$

Here, d represents the number of channels in the token, and the $\odot$ symbol denotes the Hadamard product operation.

Finally, the outputs of both are concatenated and integrated with a fully connected layer to achieve information aggregation.

$$\begin{aligned} X_t &= \mathbf{Concat}\left(X_{\text{local}}, X_{\text{global}}\right) \\ X_{\text{out}} &= \mathbf{FC}\left(X_t\right) \end{aligned} \tag{15}$$

The ConvFFN is a convolution-based feedforward neural network, consisting of two convolution layers, one depthwise convolution layer, and a dropout layer. The purpose of this design is to further extract features and to regularize through the use of the dropout layer, thereby avoiding overfitting.

C. Improved Capsule Network

Capsule networks are a vector neuron-based network architecture that consists of an encoder and a decoder [22]. The encoder includes a convolutional input layer, primary capsule layer, and digit capsule layer, primarily functioning to extract features from images and convert them into a set of dynamic vectors. The decoder comprises a fully connected layer, decoding capsule layer, and reconstruction layer, tasked with inversely reconstructing the vectors produced by the encoder back into images.

In the encoder phase, the capsule network utilizes a dynamic routing mechanism, as illustrated in Fig. 3, completed iteratively. This method implements vector clustering through a special squash($\mathbf{s}$) function, detailed in Algorithm. 1.

In the decoder phase, the original capsule network employs three fully connected layers to reconstruct the output vector to the input size, primarily comparing parameter values. This method, focusing solely on parameter differences between the reconstructed and input data, overlooks structural discrepancies. To resolve this, we've developed a three-layer deconvolution reconstruction module that captures both quantitative and structural information in its results.

D. Loss Functions

Capsule networks use feature vectors from the digit capsule layer for classification and reconstruction, involving both classification and reconstruction losses. This study redesigns the reconstruction loss, using Maximum Mean Discrepancy (MMD) to better incorporate global features into the output vectors.

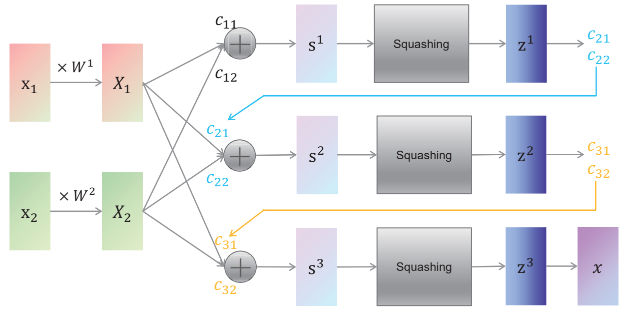

Fig. 3: Dynamic routing iteration logic.

Classification Loss: The classification loss continues to utilize the originally designed Margin Loss, which has demonstrated good performance in multi-class classification for capsule networks. The detailed formula is as follows.

$$\begin{aligned}\text{Margin Loss} &= T_k \max\left(0, m^+ - \|v_k\|\right)^2 \\ &+\lambda\left(1-T_k\right)\max\left(0, \|v_k\| - m^-\right)^2\end{aligned} \tag{16}$$

- $\|v_k\|$ represents the magnitude of the output vector of the capsule for category k. The larger the magnitude, the higher the probability of predicting that category.
- T_k is an indicator that takes the value of 1 when category k is the correct predicted category, otherwise takes 0.
- m^+ and m^- are predefined hyperparameters that represent the threshold activation values for positive and negative classes, respectively. In this study, m^+ is set to 0.9 to ensure that the capsule neurons of the correct category have sufficiently high activation levels, thereby strengthening the model's confidence in recognizing the correct category; m^- is set to 0.1 to ensure that the activation levels of capsule neurons for incorrect categories remain low, reducing misclassification.
- λ is a balancing coefficient used to weigh the contributions of positive and negative categories in the total loss. Considering that the number of positive and negative categories in this study is equal, its value is set to 0.5.

The Margin Loss effectively enhances the model's recognition efficiency for different categories by adjusting the activation levels of the capsules for each category, thereby improving the model's learning performance and robustness.

Reconstruction Loss: The reconstruction loss in this study is designed based on MMD with a global measure kernel function. MMD is specifically used to measure the difference between two data distributions.

For two given sets of samples x_i and y_i, originating from distributions P and Q respectively, MMD is defined based on the mean difference in feature space, as follows.

$$\mathrm{MMD}^2(P,Q) = \left\|\frac{1}{n}\sum_{i=1}^{n}\phi\left(x_i\right) - \frac{1}{m}\sum_{i=1}^{m}\phi\left(y_i\right)\right\|^2 \tag{17}$$

Here, ϕ is a function that maps to the Reproducing Kernel Hilbert Space (RKHS). Thus, MMD can compute the distance between the mean of samples from two distributions in feature space. By introducing the kernel function $k(x,y)$, MMD can be simplified to calculate the sample disparity between distributions P and Q.

$$\begin{aligned}\mathrm{MMD}^2(P,Q) =& \frac{1}{n^2}\sum_{i=1}^{n}\sum_{j=1}^{n}K\left(x_i,x_j\right) - \frac{2}{nm}\sum_{i=1}^{n}\sum_{j=1}^{m}K\left(x_i,y_j\right) \\ &+ \frac{1}{m^2}\sum_{i=1}^{m}\sum_{j=1}^{m}K\left(y_i,y_j\right)\end{aligned} \tag{18}$$

In this study, based on the sample characteristics and design requirements, we have co-designed three types of kernel functions to map the local, global, and dynamic similarities between targets.

Local Similarity: We use the Gaussian kernel to calculate local similarity differences due to its high sensitivity to the Euclidean distance between input points. The value of the Gaussian kernel approaches 1 when points are close and quickly decreases to 0 as their distance increases. The formula is as follows:

$$k_{\text{Gaussian}}(x,y) = \exp\left(-\frac{\|x-y\|^2}{2\sigma^2}\right) \tag{19}$$

where the parameter σ is taken as 1.0 for the width index of the nucleus.

Global Similarity: By incorporating a polynomial kernel to calculate the high-order interaction characteristics of points, data is elevated to a higher-dimensional space, effectively capturing the global structure and non-linear relationships of the data. The specific formula is as follows:

$$k_{\text{Polynomial}}(x,y) = \left(x^T y + c\right)^d \tag{20}$$

c is a linear constant (usually set to 1), and d is the degree of the polynomial. In this experiment, based on the three-dimensional features (time, frequency, amplitude) of the time-frequency image, d is set to 3.0.

Dynamic Similarity: In this study, we capture the frequency components of the original signal by introducing a Fourier kernel, facilitating the processing of dynamic patterns in time series signals. The specific formula is as follows:

$$k_{\text{Fourier}}(x,y) = \exp\left(i\omega^T(x-y)\right) \tag{21}$$

Finally, by integrating these three kernel functions, we obtain the MMD Loss designed in this study.

$$k_{\text{out}} = \frac{k_{\text{Gaussian}} \cdot k_{\text{Polynomial}} \cdot k_{\text{Fourier}}}{k_{\text{Gaussian}} + k_{\text{Polynomial}} + k_{\text{Fourier}}} \tag{22}$$

$$\begin{aligned}\text{MMD Loss} =& \frac{1}{n^2}\sum_{i=1}^{n}\sum_{j=1}^{n}k_{\text{out}}\left(x_i,x_j\right) - \frac{2}{nm}\sum_{i=1}^{n}\sum_{j=1}^{m}k_{\text{out}}\left(x_i,y_j\right) \\ &+ \frac{1}{m^2}\sum_{i=1}^{m}\sum_{j=1}^{m}k_{\text{out}}\left(y_i,y_j\right)\end{aligned} \tag{23}$$

Loss Consolidation: Due to the different magnitudes of these two loss functions, to ensure that the reconstructed features effectively influence the classification results without overshadowing the original classification mechanism, this study employs a logarithmic function to normalize the MMD

Algorithm 1 Dynamic Routing

Input: output vectors u_i for all capsules i in layer l, number of routing iterations r
Output: activation vectors v_j for all capsules j in layer $l+1$
Initialize log priors $b_{ij} \leftarrow 0$ for all capsule pairs i, j
for $t = 1$ **to** r **do**
  for each capsule i in layer l **do**
    Predicted vectors $x_{ij} \leftarrow u_i W_{ij}$
  end for
  for each capsule i in layer l **do**
    Compute coupling coefficients $c_{ij} \leftarrow \text{softmax}(b_{ij})$
  end for
  for each capsule j in layer $l+1$ **do**
    Compute total input vectors $s_j \leftarrow \sum_i c_{ij} x_{ij}$
    Apply squash function $v_j \leftarrow \text{squash}(s_j)$
  end for
  if $t < r$ **then**
    for each capsule i in layer l and capsule j in layer $l+1$ **do**
      Update log priors $b_{ij} \leftarrow b_{ij} + x_{ij} \cdot v_j$
    end for
  end if
end for
Define squash function: $\text{squash}(\mathbf{s}) = \frac{\|S_j^2\|}{1+\|S_j^2\|} \frac{S_j}{\|S_j\|}$

loss. This approach allows for a more balanced consideration of the impacts of both types of losses when they are integrated.

$$\text{Reconstruction Loss} = ln\left(\sqrt{\text{MMD Loss}}\right) \tag{24}$$

$$\text{Loss} = \text{Margin Loss} + a \cdot \text{Reconstruction Loss} \tag{25}$$

where a denotes the reconstruction ratio. Through the interaction of the two types of losses, we achieve a global supervision of local effects, ensuring that the output vector contains both high-frequency and low-frequency features of the original signal.

IV. Experimental verification

A. Experimental Environment

Hardware Environment: The model training was conducted on a platform equipped with an NVIDIA GeForce RTX 3090 GPU and an Intel Core i9-12900K CPU.

Software Environment: The experiments were executed on a Linux operating system. The development environment was based on the Pytorch 2.0-GPU framework, selected for its comprehensive library support and GPU capabilities.

Model Parameters: Lion optimizer was employed for its robust performance characteristics. The model underwent training with a batch size of 32 over 50 epochs. An initial learning rate of 0.0002 was set, with a learning rate decay of 0.8 implemented every 10 epochs to ensure steady convergence of the model.

The experimental circuit is built using the LM2596S integrated chip, with component parameters detailed in Table I. The parasitic aging parameters of the components are monitored using an LCR Meter. The experimental platform is illustrated in Fig. 4. During the data acquisition phase, a DSOX3024T oscilloscope is used to capture the output ripple voltage of the circuit under various operating conditions. Model testing is conducted on an edge computing platform, built around the NVIDIA JETSON Nano and NI-6001 data acquisition card.

TABLE I: CIRCUIT COMPONENT PARAMETERS

Circuit	f_s	C_o	C_b	L_1	L_2	R
Buck	100kHz	47μF	\	220μH	\	5Ω
Superbuck	100kHz	47μF	100μF	220μH	220μH	5Ω

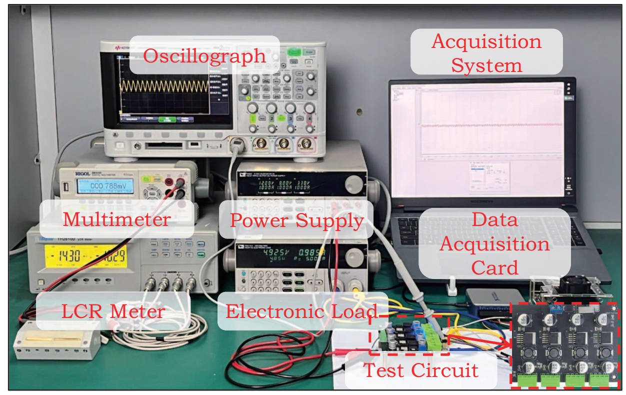

Fig. 4: Hardware experimental platform.

B. Fault Data Definition

To ensure that the dataset accurately reflects the actual state of the DC-DC converter at different stages of failure, this experiment was conducted based on the Arrhenius thermal aging test for output capacitors. The Arrhenius equation is expressed as follows:

$$k = A - E_a/(R \cdot T) \tag{26}$$

where k represents the reaction rate constant, A is the pre-exponential factor, E_a is the activation energy, R is the universal gas constant ($8.314 J/mol \cdot K$), and T represents the temperature. In our study, we use the reaction rate constant k to describe the ratio of the aging capacitor's circuit output voltage ripple a to the initial thermal aging time. Utilizing this function, we were able to derive the fitted values of $k(Buck)$ and $k(Superbuck)$ and calculate the predicted aging time at any given temperature. In this study, we set 423.15K as the accelerated aging temperature. The range where the output voltage ripple ratio changes from 1% to 10% is defined as the hidden fault state. Voltage ripple ratio (V_{rr}) below 1% is considered normal, while above 10% indicates complete damage to the DC-DC power supply. The data collection results for the two circuits at different fault levels are presented in Table II.

For each of the ten states of each circuit type, a $10ms$ output signal was collected and subjected to adaptive wavelet transformation, converting it into a time-frequency image dataset, as shown in Fig. 5.

C. Data Processing Experiment

To validate the scientific soundness and effectiveness of the AWT for time-frequency transformations, this study introduces a distinctiveness measure D based on the theory of gray-level co-occurrence matrices (GLCM) [23].

TABLE II: CONVERTERS FAILURE RATINGS DATA

Circuit	Level	Time(h)	C(μF)	ESR(Ω)	$\mathbf{V_{rr}}$(%)
Buck	0	0	43.82	0.297	0.667
	1	14.10	42.93	0.693	1.552
	2	22.50	41.51	1.301	2.531
	3	30.25	40.89	2.112	3.482
	4	36.30	39.86	3.382	4.523
	5	39.75	38.92	4.850	5.496
	6	43.10	36.92	6.123	6.473
	7	46.25	36.52	7.439	7.528
	8	48.60	35.23	8.961	8.498
	9	49.50	35.13	9.830	9.513
Superbuck	0	0	114.89	0.114	0.502
	1	8.75	113.65	0.380	1.513
	2	14.50	112.16	0.625	2.526
	3	19.25	110.47	0.913	3.544
	4	22.50	106.82	1.253	4.517
	5	25.00	103.20	1.408	5.533
	6	27.10	100.68	1.936	6.496
	7	29.25	96.37	2.484	7.521
	8	31.00	93.17	3.361	8.548
	9	32.30	91.84	4.103	9.552

$k(Buck)$: A=2.295, E_a =10790.53J/mol
$k(Superbuck)$: A=2.352, E_a =9077.45J/mol

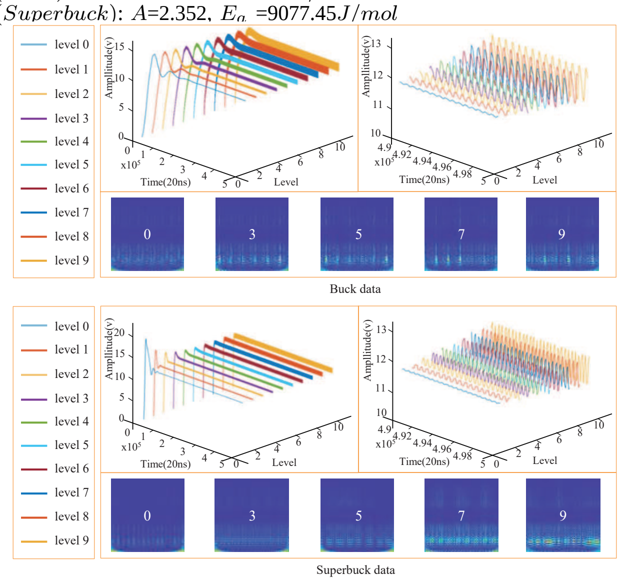

Fig. 5: Converters fault time-frequency image.

Initially, for each time-frequency image P, we compute the statistical measures from its GLCM, including contrast (CO), dissimilarity (DI), homogeneity (HO), and energy (EN) [24], to form a feature vector $\mathbf{F}$.

$$\mathbf{F} = [CO\,(P)\,, DI\,(P)\,, HO\,(P)\,, EN\,(P)] \tag{27}$$

Next, calculate the intra-class and inter-class distances respectively:

$$\text{Intra} = \frac{1}{N(N-1)} \sum_{i=1}^{N} \sum_{j=i+1}^{N} \|\mathbf{F}_i - \mathbf{F}_j\| \tag{28}$$

$$\text{Inter} = \frac{2}{C(C-1)} \sum_{a=1}^{C} \sum_{b=a+1}^{C} \frac{1}{N^2} \sum_{i=1}^{N} \sum_{j=1}^{N} \left\|\mathbf{F}_a^i - \mathbf{F}_b^j\right\| \tag{29}$$

In the formula, N represents the number of samples within a class, C denotes the total number of classes, and the term represents the Euclidean distance between feature vectors. From this, the distinctiveness D can be calculated.

$$D = \frac{\text{Inter}}{\frac{1}{C}\sum \text{Intra}} \tag{30}$$

The greater the distinctiveness D, the better the transformation effect, making the time-frequency images more conducive for the model to perform classification and diagnosis. In the experiments, Short-Time Fourier Transform (STFT), Wigner-Ville Transform, CWT, and AWT are compared. The Buck circuit dataset is used as an example to transform and compute 100 time-frequency images for each category. The experimental results are shown in Fig 6. For clarity in presentation, the image resolution displayed here is 2000×2000, while the actual input image size for the model is 64×64.

The STFT has poor time-frequency resolution and performs inadequately on datasets, failing to effectively reveal fault characteristics. Although the Wigner-Ville Transform introduces cross-terms, which increase the amount of features, this also complicates the calculation of distinctiveness, resulting in suboptimal performance. The CWT demonstrates better performance, particularly offering higher frequency resolution in the low-frequency components of the signal, thus reflecting a certain degree of fault discrimination. However, the fixed-scale wavelet computation in CWT leads to the loss of fault point information, failing to comprehensively reflect changes in the signal. In contrast, the AWT method shows excellent time-frequency focusing in both high and low frequency parts, effectively displaying the distinctiveness of electrical signal faults in the time-frequency domain, thereby better capturing fault characteristics.

D. Model Validation Experiment

In the initial training stages, the model was influenced by two hyperparameters: the number of dynamic routing iterations and the reconstruction loss coefficient. Preliminary experiments using Buck circuit data helped determine the optimal settings, detailed in Table III.

Taking into account the loss and accuracy of the validation set, we observed that the optimal performance is achieved with three iterations of dynamic routing, and the best results are obtained when the reconstruction loss coefficient is set to 0.4.

The pre-training process of the model is illustrated in Fig 7 and Fig 8. In these two datasets, the XCCN model essentially completed its iterative learning between 15 to 20 epochs, with accuracy rising to 96%. Due to the slightly higher complexity of the Superbuck dataset compared to the Buck dataset, its training progress was delayed by about 5 epochs. When the training rounds reached 50 epochs, the model achieved its highest validation accuracy, at 99.28% and 98.72% respectively. Additionally, the loss function of the model steadily decreased throughout the training phase, confirming that the loss function settings were appropriate and that the model did not exhibit overfitting during the training process.

To comprehensively evaluate and compare the XCCN model proposed in this study with other models, in addition to conventional accuracy, we also introduced the following three key indicators:

$$\begin{cases} P = TP/(TP+FP) \\ R = TP/(TP+FN) \\ HA = 2P \times R/(P+R) \end{cases} \tag{31}$$

Among these, Harmonic Accuracy (HA) is the harmonic mean of Precision Ratio (P) and Recall Rate (R). The calculations for P and R are based on the identification of True

TABLE IV: MODEL PERFORMANCE COMPARISON DATA SHEET

Model	Buck					Superbuck					Performance Indicators	
	Accuracy(%)	Time(s)	P	R	HA	Accuracy(%)	Time(s)	P	R	HA	PS(MB)	IT(s/100)
SVM	93.35	0.31	93.28	92.13	92.70	88.13	0.29	85.05	84.14	84.59	2.71	1.159
1DCNN	96.43	5.58	96.42	94.82	95.61	90.93	6.81	83.27	86.79	84.99	8.76	5.282
LSTM	81.58	7.32	80.25	83.64	81.91	79.88	8.96	76.94	77.68	73.78	6.21	7.465
GRU	92.61	8.48	91.08	89.84	90.46	87.62	11.12	77.64	75.93	82.31	4.76	2.173
CNN	97.03	168.64	96.59	96.51	96.55	95.04	193.49	93.33	92.09	92.71	24.54	7.908
VIT	95.43	225.51	93.28	91.63	93.87	93.57	249.35	94.82	90.25	91.64	35.13	8.313
CCN	90.83	297.45	88.98	90.04	89.51	91.01	342.22	89.85	90.15	90.00	33.25	8.143
XCCN	**99.28**	**328.82**	**99.61**	**98.93**	**99.27**	**98.72**	**401.55**	**97.82**	**97.24**	**97.53**	**41.23**	**9.125**

One-dimensional data processing model: SVM, 1DCNN, LSTM, GRU.
Two-dimensional image processing model: CNN, VIT, CCN, **XCCN**.
PS: Parameter Size, used to measure the complexity and scale of a model.
IT: Inference Time, used to gauge the model's real-time performance and efficiency.

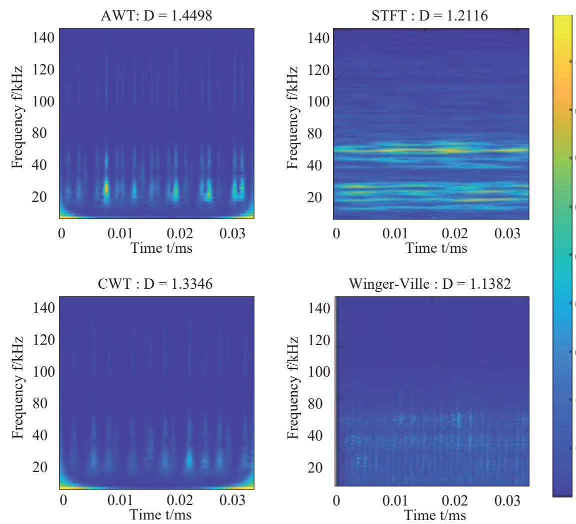

Fig. 6: Comparison of distinctiveness.

TABLE III: HYPERPARAMETER PERFORMANCE

Iterations	Reconstruction ratio	Accuracy(%)	Loss
1	0.3	96.2	0.8532
1	0.4	97.5	0.7858
1	0.5	97.1	0.8038
2	0.3	97.5	0.7769
2	0.4	98.3	0.6823
2	0.5	97.8	0.7657
3	0.3	98.6	0.6325
3	**0.4**	**99.28**	**0.6113**
3	0.5	98.9	0.6234

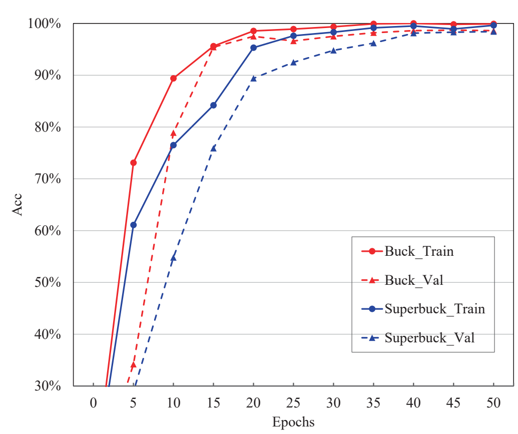

Fig. 7: Traing and validation acc.

Positive instances (TP), False Positive instances (FP), and False Negative instances (FN).

Comparative experimental results are presented in Table IV. In the one-dimensional data processing model, 1DCNN demonstrated superior performance, achieving an accuracy of 96.43% on the Buck circuit and 90.93% on the Superbuck circuit, outperforming SVM, GRU, and LSTM. However, two-dimensional image processing models generally showed higher diagnostic accuracy than one-dimensional models. Among them, CNN slightly outperformed VIT due to its tendency to ”overfit” local features, which provides an advantage when the dataset is simple. In contrast, the original CCN performed poorly in direct diagnostics, with accuracies only around 90% for both circuits. Conversely, the XCCN model made a significant breakthrough in accuracy, exceeding 98% on both the Buck and Superbuck circuits.

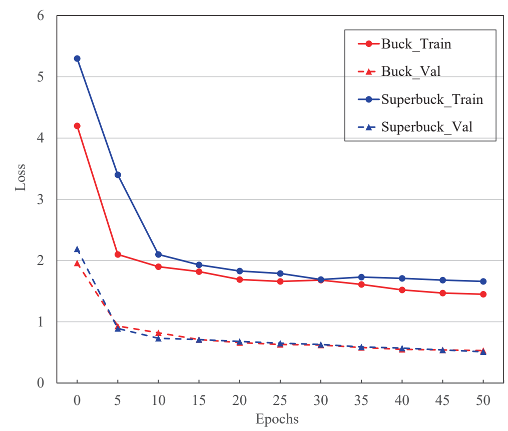

Fig. 8: Traing and validation loss.

Additionally, performance indicators show that two-dimensional image processing models are generally more complex than one-dimensional models. The XCCN model has slightly more parameters than other two-dimensional models. In terms of execution speed, XCCN's Inference Time (IT) is about 1 second slower on average than other two-dimensional models, but the difference per image is only 0.01 seconds. Experimental results demonstrate that the XCCN model outperforms existing deep learning models used in fault diagnosis in terms of overall model performance.

E. Hardware Comparison Experiment

In this experiment, the diagnostic performance of the AWT-XCCN method was tested under varying load conditions. Under the fault conditions set in Table II, we adjusted the load size of the converter to simulate changes in the operating state, conducting a variable load experiment. The structure of the diagnostic tasks is detailed in Table V. A comprehensive comparison of four methodsCWT-CNN, CWT-VIT, CWT-XCCN,

TABLE V: VARIABLE LOAD DIAGNOSTIC TASKS

Datasets	Loads	STSE		DTSE	
		Train	Test	Train	Test
A	2.5Ω	A	BC	AB	C
B	5Ω	B	AC	AC	B
C	7.5Ω	C	AB	BC	A

STSE: Single-training-set experiment
DTSE: Dual-training-set experiment

and AWT-XCCNwas carried out, with the experimental results presented in Fig 9.

In the single dataset experiment, the traditional CWT-CNN method only achieved an average accuracy of 67.65% due to its inability to effectively match the learned local features, particularly when there was a significant load difference between the dataset and the test set. However, when the diagnostic model was switched to XCCN and VIT, there was a significant improvement in diagnostic performance, with XCCN slightly outperforming VIT. Ultimately, with the introduction of the AWT method, forming the AWT-XCCN approach of this study, the average accuracy reached 93.04%.

In the dual dataset experiment, the overall trends were similar to those of the single dataset experiment. With the addition of more datasets and types, providing a greater number of local similar features, both the traditional CWT-CNN method and the CWT-XCCN method, which used CWT data processing method, improved their accuracy by 4%. CWT-VIT, which was most sensitive to the number of datasets, achieved 93.25% accuracy. In contrast, the AWT-XCCN method of this study ultimately reached an average accuracy of 96.33%.

In summary, the hardware comparison experiment results demonstrate that the methods developed in this study achieve the highest average accuracy when circuit operational states change, better adapting to fault conditions that occur during actual circuit operations. This shows superior generalization capability and robustness.

V. Conclusion

This study has addressed a key issue in fault diagnosis of DC-DC converters, which is the neglect of the temporal continuity of electrical signals. We have introduced the AWT method, integrating EMD, HHT with CWT for dynamic adjustment of scale and translation parameters. A specialized XCCN has been developed, focusing on global features and enhancing fault diagnosis through advanced processing techniques. Tests on Buck and Superbuck circuits have validated the XCCN model's superiority in diagnostic accuracy, harmonic accuracy, and recall rate. Overall, our developed innovative approach has shown significant improvements over traditional methods, paving the way for future research on its application to other converters and real-time fault detection in various industries.

Future work will focus on evaluating the adaptability of this method across different types of converters and exploring its capabilities for real-time fault detection in various industrial settings. This includes using spectral residual-based anomaly detection [25], implementing privacy-preserving federated learning [26] [27], and optimizing residual generators [28] [29]. The goal is to improve the reliability and security of industrial systems through multi-agent systems and data-driven approaches [30] [31] [32].

References

[1] S. Peyghami, Z. Wang and F. Blaabjerg, "A Guideline for Reliability Prediction in Power Electronic Converters," *IEEE Trans. Power Electron.*, vol. 35, no. 10, pp. 10958-10968, Oct. 2020.

[2] A. Dong, A. Starr and Y. Zhao, "Neural network-based parametric system identification: a review," *Int. J. Syst. Sci.*, vol. 54, no. 13, pp. 2676-2688, 2023.

[3] S. Ye, F. Zhang, F. Gao, Z. Zhou and Y. Yang, "Fault Diagnosis for Multilevel Converters Based on an Affine-Invariant Riemannian Metric Autoencoder," *IEEE Trans. Ind. Informat.*, vol. 19, no. 3, pp. 2619-2628, Mar. 2023.

[4] X. Zhou, N. Zhai, S. Li and H. Shi, "Time Series Prediction Method of Industrial Process With Limited Data Based on Transfer Learning," *IEEE Trans. Ind. Informat.*, vol. 19, no. 5, pp. 6872-6882, May 2023.

[5] W. Luo et al., "Fault Diagnosis Method Based on Two-Stage GAN for Data Imbalance,"*IEEE Sensors J.*, vol. 22, no. 22, pp. 21961-21973, Nov. 2022.

[6] W. He, Y. He, B. Li and C. Zhang, "A Naive-Bayes-Based Fault Diagnosis Approach for Analog Circuit by Using Image-Oriented Feature Extraction and Selection Technique," *IEEE Access*, vol. 8, pp. 5065-5079, July 2019.

[7] C. Zhang et al., "An Analog Circuit Fault Diagnosis Approach Based on Improved Wavelet Transform and MKELM," *Circuits Syst. Signal Process.*, vol. 41, pp. 1255-1286, Jan. 2022.

[8] S. Feng, X. Li, S. Zhang, Z. Jian, H. Duan and Z. Wang, "A review: state estimation based on hybrid models of Kalman filter and neural network," *Syst. Sci. Control Eng.*, vol. 11, no. 1, art. no. 2173682, 2023.

[9] H. Yang, C. Meng and C. Wang, "Data-Driven Feature Extraction for Analog Circuit Fault Diagnosis Using 1-D Convolutional Neural Network," *IEEE Access*, vol. 8, pp. 18305-18315, Jan. 2020.

[10] L. Ji, C. Fu and W. Sun, "Soft Fault Diagnosis of Analog Circuits Based on a ResNet With Circuit Spectrum Map," *IEEE Trans. Circuits Syst. I, Reg. Papers*, vol. 68, no. 7, pp. 2841-2849, July 2021.

[11] X. Li, S. Wan and S. Liu, "Bearing Fault Diagnosis Method Based on Attention Mechanism and Multilayer Fusion Network," *ISA Trans.*, vol. 128, Part B, pp. 550-564, Sept. 2022.

[12] S. Zhang, Z. Liu, Y. Chen, "Selective Kernel Convolution Deep Residual Network Based on Channel-Spatial Attention Mechanism and Feature Fusion for Mechanical Fault Diagnosis," *ISA Trans.*, vol. 133, pp. 369-383, Feb. 2023.

[13] M. Huang, J. Yin, S. Yan and P. Xue, "A Fault Diagnosis Method of Bearings Based on Deep Transfer Learning," *Simul. Model. Pract. Th.*, vol. 122, no. 102659, Jan. 2023.

[14] J. Liao, H.-K. Lam, S. Gulati and B. Hayee, "Improved computer-aided diagnosis system for nonerosive reflux disease using contrastive self-supervised learning with transfer learning," *Int. J. Netw. Dyn. Intell.*, vol. 2, no. 3, art. no. 100010, Sep. 2023.

[15] S. Zhang, R. Wang, Y. Si and L. Wang, "An Improved Convolutional Neural Network for Three-Phase Inverter Fault Diagnosis," *IEEE Trans. Instrum. Meas.*, vol. 71, pp. 1-15, Nov. 2021.

[16] B. Yang, R. Liu and E. Zio, "Remaining Useful Life Prediction Based on a Double-Convolutional Neural Network Architecture," *IEEE Trans. Ind. Electron.*, vol. 66, no. 12, pp. 9521-9530, Dec. 2019.

[17] Y. Zhou, Y. Guo, C. Liu, H. Peng and H. Rao, "Synchronization for Markovian master-slave neural networks: an event-triggered impulsive approach," *Int. J. Syst. Sci.*, vol. 54, no. 12, pp. 2551-2565, 2023.

[18] A. Mobiny, H. Lu, H. V. Nguyen, B. Roysam and N. Varadarajan, "Automated Classification of Apoptosis in Phase Contrast Microscopy Using Capsule Network," *IEEE Trans. Med. Imag.*, vol. 39, no. 1, pp. 1-10, Jan. 2020.

[19] J. Gu, Y. Peng, H. Lu, X. Chang, and G. Chen, "A Novel Fault Diagnosis Method of Rotating Machinery via VMD, CWT and Improved CNN," *Measurement*, vol. 200, no. 111635, Aug. 2022.

[20] Y. Hou, Y. Zhang, J. Lu, N. Hou and D. Yang, "Application of improved multi-strategy MPA-VMD in pipeline leakage detection," *Syst. Sci. Control Eng.*, vol. 11, no. 1, art. no. 2177771, 2023.

[21] Q. Fan, H. Huang, J. Guan and R. He, "Rethinking Local Perception in Lightweight Vision Transformer," 2023, *arXiv:2303.17803*. [Online]. Available: http://arxiv.org/abs/2303.17803

[22] G. Yang, H. Tao, R. Du and Y. Zhong, "Compound Fault Diagnosis of Harmonic Drives Using Deep Capsule Graph Convolutional Network," *IEEE Trans. Ind. Electron.*, vol. 70, no. 4, pp. 4186-4195, Apr. 2023.

[23] L. Shao, J. He, X. Lu, B. Hei, J. Qu, and W. Liu, "Aircraft Skin Damage Detection and Assessment From UAV Images Using GLCM and Cloud Model," *IEEE Trans. Intell. Transp. Syst.*, vol. 25, no. 3, pp. 3191-3200, Mar. 2024.

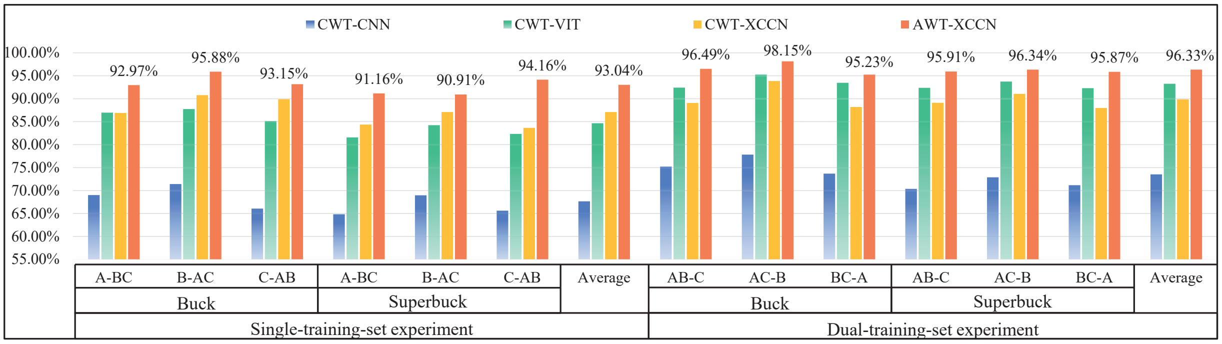

Fig. 9: Variable load experiment.

[24] Z.-Y. Li, J. Hyttinen, R. Risnen, X.-Z. Gao and M. Hauta-Kasari, "Unsupervised spectral analysis of bio-dyed textile samples," *Int. J. Netw. Dyn. Intell.*, vol. 2, no. 2, art. no. 100001, Jun. 2023.

[25] T. Xie, Q. Xu, C. Jiang, Z. W. Gao and X. Wang, "A robust anomaly detection model for pumps based on the spectral residual with self-attention variational autoencoder," *IEEE Trans. Ind. Informat.*, vol. 20, no. 6, pp. 9059-9069, Jun. 2024.

[26] S. Lu, Z. W. Gao, Q. Xu, C. Jiang, A. Zhang, and X. Wang, "Class-imbalance privacy-preserving federated learning for decentralized fault diagnosis with biometric authentication," *IEEE Trans. Ind. Informat.*, vol. 18, no. 12, pp. 9101-9111, Dec. 2022.

[27] M. Wei, M. Huang and J. Ni, "Cross-subject EEG channel selection method for lower limb brain-computer interface," *Int. J. Netw. Dyn. Intell.*, vol. 2, no. 3, art. no. 100008, Sep. 2023.

[28] Y. Jiang, S. Yin and O. Kaynak, "Optimized design of parity relation-based residual generator for fault detection: data-driven approaches," *IEEE Trans. Ind. Informat.*, vol. 17, no. 2, pp. 1449-1458, Feb. 2021.

[29] M. I. Khedher, H. Jmila and M. A. El-Yacoubi, "On the formal evaluation of the robustness of neural networks and its pivotal relevance for AI-based safety-critical domains," *Int. J. Netw. Dyn. Intell.*, vol. 2, no. 4, art. no. 100018, Dec. 2023.

[30] C. Wang, Z. Wang, Q. Liu, H. Dong and W. Sheng, "Support-sample-assisted domain generalization via attacks and defenses: concepts, algorithms, and applications to pipeline fault diagnosis," *IEEE Trans. Ind. Informat.*, vol. 20, no. 4, pp. 6413-6423, Apr. 2024.

[31] C. Wang, Z. Wang, L. Ma, H. Dong and W. Sheng, "Subdomain-alignment data augmentation for pipeline fault diagnosis: an adversarial self-attention network," *IEEE Trans. Ind. Informat.*, vol. 20, no. 2, pp. 1374-1384, Feb. 2024.

[32] B. Liu, X. Shen, L. Wu, and H. Su, "Observability of Heterogeneous Multi-Agent Systems," *IEEE Trans. Netw. Sci. Eng.*, vol. 8, no. 2, pp. 1828-1841, Apr. 2021.

Li Wang (Member, IEEE) received the Ph.D. degree in control science and engineering from the College of Electronics and Information Engineering, Tongji University, Shanghai, China, in 2019. He has published over 20 scientific papers in journals and international conferences. He is currently a Lecturer and a Graduate Advisor with the School of Electrical Engineering and Automation, Nantong University, Nantong, China. His research interests focus on the prognostics and health management of power electronic circuits, advanced measurement and control technologies, failure diagnosis algorithms, and design for embedded systems.

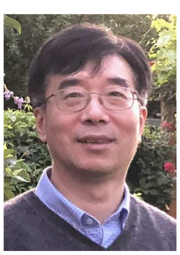

Zidong Wang (Fellow, IEEE) is currently a Professor of dynamical systems and computing with the Department of Computer Science, Brunel University London, Uxbridge, U.K. He has authored a number of articles in international journals. He is a member of the Academia Europaea and the European Academy of Sciences and Arts, an Academician of the International Academy for Systems and Cybernetic Sciences, a fellow of the Royal Statistical Society, and a member of the program committee for many international conferences. He serves (or has served) as the Editor-in-Chief for International Journal of Systems Science, Neurocomputing, and Systems Science and Control Engineering.

Chao Xu (Student Member, IEEE) received the B.S. degree in Electrical Engineering and Automation from Nantong University, Jiangsu, China, in 2017. Since June 2022, he has been pursuing a Master's degree in Control Science and Engineering at Nantong University in Jiangsu, China. His research interests include failure detection of power electronic converters, on-line health monitoring technology, deep learning and embedded system design.

Yiming Xu received the Ph.D. degree in 2011 from Nanjing University of Science and Technology, specialising in weapons science and technology. In 2015, he joined a Faculty Member of Nantong University, where he is currently a Professor of Electrical Engineering. He is a member of the Youth Working Committee of the Chinese Society of Automation, Specialised Committee on Cognitive Computing, Information Processing and Systems, Chinese Society of Artificial Intelligence. He has published 30 papers in SCI/EI journals. His research interests include electrical equipment detection and safe operation, machine vision intelligent perception and FBG sensing technology.

Liang Hua received the B.S. degree in the School of Electrical Engineering and Automation from Nantong University, Nantong, China, in 2001, and the M.S. and Ph.D. degrees in control engineering from the Zhejiang University of Technology, Hangzhou, China, in 2008 and 2014, respectively. In 2001, he joined a Faculty Member of Nantong University, where he is currently a Professor of Electrical Engineering. He is a member of the Youth Working Committee of the Chinese Society of Automation. His research interests include power system optimization, renewable power generation, and energy storage systems.